Article

A Novel Permeability–Tortuosity–Porosity Model for Evolving Pore Space and Mineral-Induced Clogging in Porous Medium

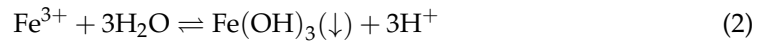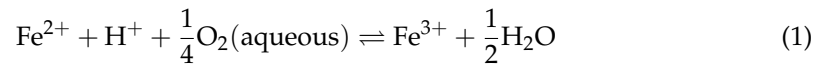Wenran Cao [1,*], Guanxi Yan [2,*], Harald Hofmann [3,4] and Alexander Scheuermann [2]

1   Sustainable Minerals Institute, University of Queensland, Brisbane, QLD 4072, Australia
2   School of Civil Engineering, University of Queensland, Brisbane, QLD 4072, Australia;
    a.scheuermann@uq.edu.au
3   Environment, Commonwealth Scientific and Industrial Research Organisation (CSIRO),
    Brisbane, QLD 4102, Australia; harald.hofmann@csiro.au or h.hofmann@uq.edu.au
4   School of the Environment, University of Queensland, Brisbane, QLD 4072, Australia
*   Correspondence: wenran.cao@uq.edu.au (W.C.); g.yan@uq.edu.au (G.Y.)

Abstract: Hydrogeochemical processes contribute to long-term alterations in key physical properties of a porous medium, including porosity, tortuosity, and permeability, making it essential to understand their evolution and address clogging-dominated problems in hydrogeological systems such as acid rock drainage treatment and aquifer storage and recovery. However, accurately simulating extreme cases of evolving pore space presents challenges due to the inherent heterogeneity and nonlinear reactions in a porous medium. In response, this study introduces a comprehensive model that integrates the effects of tortuosity on permeability and surface area on reactivity during oxidative precipitation of Fe(II) in a porous medium. Benchmark simulations include an innovative permeability–tortuosity–porosity model accounting for Fe precipitation, as well as the occurrence of complete clogging from localized precipitation, which leads to a reduction of permeability and outflow. The outcomes demonstrate complete pore clogging when Fe(II) concentration reaches 10 mmol/L and a significant decrease in outflow at a Fe(II) concentration of 100 mmol/L. The model's predictions provide detailed insights into the evolution of the pore matrix during hydrogeochemical reactions and support the development of regional engineering-scale models for applications in mining, agriculture, and environmental management.

Keywords: porous medium; oxidative precipitation of Fe(II); permeability–tortuosity–porosity model; pore clogging; reactive transport modeling

1. Introduction

Australia has the greatest global reserves of iron (Fe) ore [1], and Fe ions can readily enter aquatic environments through natural processes, for example, from acid sulfate soils, discharge, and anoxic groundwater or through anthropogenic processes such as industrial discharge and landfill leachate [2]. In the presence of dissolved oxygen (DO), ferrous ions (i.e., Fe(II) or Fe^{2+}) can be oxidized into ferric ions (i.e., Fe(III) or Fe^{3+}), which then precipitate as ferric hydroxides (represented as $Fe(OH)_3$) within soil [3,4] (Equations (1) and (2)). The precipitation of minerals in the pore space lead to long-term changes in soil porosity, as well as the evolution of tortuosity and permeability [5]. Therefore, determining the evolution of these parameters and managing clogging-related problems are vital for a large variety of hydrogeological systems, including acid rock drainage (ARD) treatment [6], aquifer storage and recovery (ASR) [7], engineered barrier systems (EBS) [8,9], well fouling

due to mineral precipitation [10], fluid circulation in geothermal systems [11], and deep ground repositories of high-level nuclear waste (HLW) [12,13].

$$\text{Fe}^{2+} + \text{H}^+ + \frac{1}{4}\text{O}_2(\text{aqueous}) \rightleftharpoons \text{Fe}^{3+} + \frac{1}{2}\text{H}_2\text{O} \tag{1}$$

$$\text{Fe}^{3+} + 3\text{H}_2\text{O} \rightleftharpoons \text{Fe(OH)}_3(\downarrow) + 3\text{H}^+ \tag{2}$$

Unconsolidated natural materials can be characterized as a porous medium consisting of a solid matrix and interconnected pores (or voids), which allows for fluid flow and solute transport through the pore network (Figure 1a). Mineral precipitation (for example, through Fe(II) oxidation) within the pore space reduces the pore volume, decreasing porosity, reducing permeability, and increasing tortuosity [14]. These changes consequently slow groundwater movement and solute transport [15]. Figure 1b illustrates the interactively underlying mechanisms between fluid flow, solute transport, and geochemical reactions. The conceptualization reveals that hydrogeochemical processes related to Fe(II) oxidative precipitation are inherently linked to porosity (Φ), permeability (k), and tortuosity (τ). The relationship between these parameters is formulated by the Kozeny–Carman (KC) equation (see Equation (3)). However, the shape factor (C) is typically assumed to remain constant over time, and the role of tortuosity in the evolution of permeability is often overlooked [16–19]. Studies have shown that Fe precipitation can significantly reduce pore throat size and obstruct the initial pore space [20–22], which results in higher tortuosity values and brings challenges in advective/diffusive transport. To address this critical gap, our previous research developed a novel permeability–tortuosity–porosity model that is both straightforward and geophysical meaningful [23];

$$k = \frac{1}{C}\frac{\varnothing^3}{(1-\varnothing)^2}d^2 \tag{3}$$

where d indicates the spatially averaged diameter at the scale of representative elementary volume (REV) (m).

While pore throat obstruction is the initial process, complete pore-clogging can result from the accumulation of Fe precipitates in a porous medium, causing the total disappearance of aqueous phases. This presents significant challenges for numerical simulations, as most reactive transport modeling (RTM) frameworks implement a threshold of porosity, i.e., critical value, below which seepage flow and solute transport could be assumed nonexistent [14]. Currently, there is limited research on this topic in the published literature, with notable exceptions being the coupled OpenFOAM–PHREEQC platform developed by Soulaine et al. [24] and Pavuluri et al. [25]. Additionally, the precipitation-dominated regime is governed by the characteristic timescales for diffusion, advection, and reaction processes. Although previous studies have provided valuable insights into the coupling process between geophysics and geochemistry [26–30], it remains challenging to estimate the historical evolutions of transport parameters because they are more dependent on the precipitate spatial distribution than on their total quantity, specifically in cases of pore clogging. This highlights the inadequacy of methodologies relying on porosity alone to fully capture the complexities of geophysical and geochemical coupling processes at both microscale and macroscale (i.e., pore and continuum scales), thereby underscoring the need for a highly integrated method to determine evolving parameters for complete pore-clogging phenomena [14]. Recent research has further demonstrated that the chemical reaction rates of oxidation and precipitation are predominantly governed by the effective surface area [14,31,32]. High-resolution imaging has also indicated that precipitated Fe can coat existing particles without necessarily clogging pore throats [33]. Consequently, it

could be more appropriate to incorporate the surface area into models, given the inherent correlation between surface area and reactivity [34], along with the finding that a larger surface area leads to more tortuous seepage flow conduits [35].
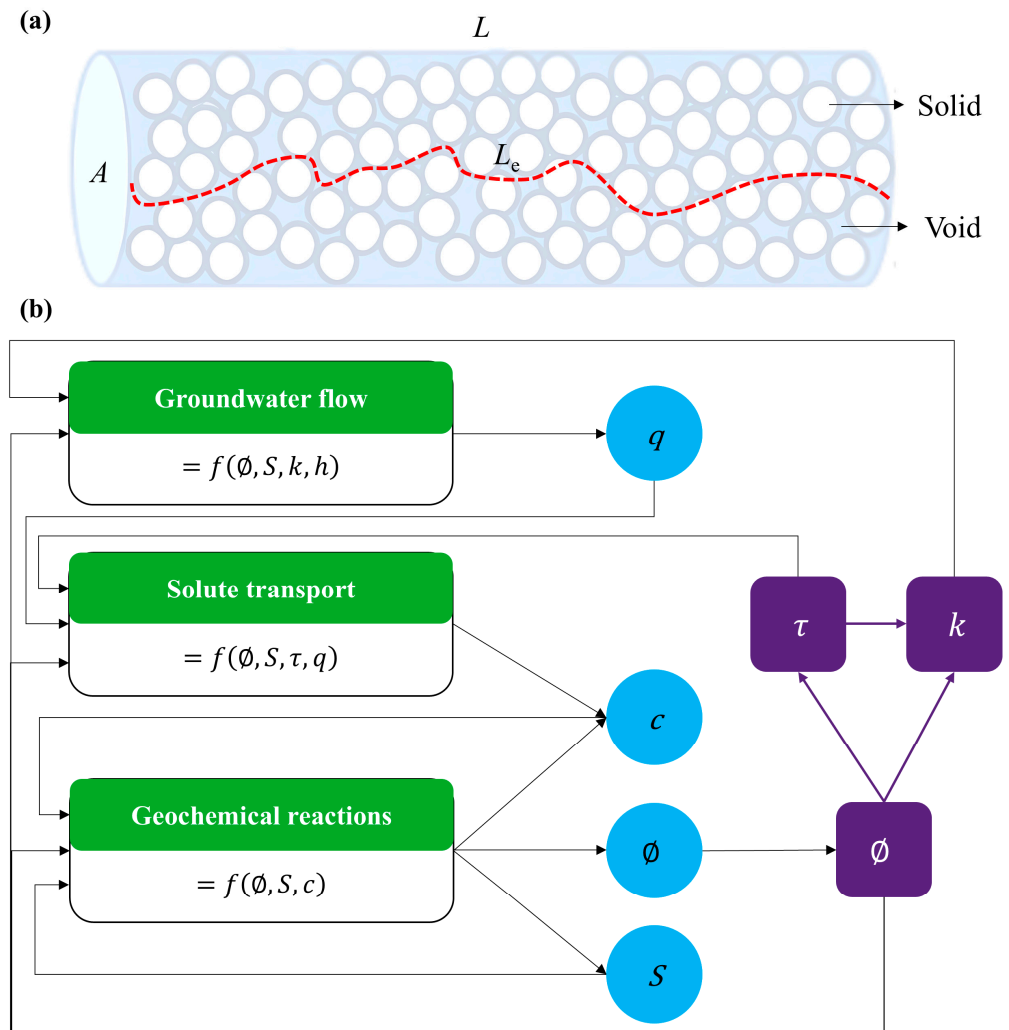

Figure 1. (**a**) Porous medium consisting of a solid matrix and interconnected pores (or voids), where A is the cross-sectional area (m^2), L is the straight-line distance from the starting to ending point (m), and L_e is the effective length of a flow channel (m); (**b**) schematic diagram of interactive mechanisms between fluid flow, solute transport, and geochemical reactions, where Φ is porosity, k is permeability (m^2), τ is tortuosity, S is surface area (m^2), h is hydraulic head (m), q is volumetric flow rate (m/s), and c is molar concentration (mol/L).

Upon our previous study on the permeability–porosity model [23], this study presents an integrated numerical model with engineering applicability that integrates the effects of tortuosity on permeability and surface area on reactivity during Fe(II) oxidative precipitation in a porous medium. The model extends the Kozeny–Carman (KC) equation by adopting a tortuosity–porosity relationship based on Archie's law while incorporating surface-controlled reactions using a power-law function. Additionally, benchmark simulations are conducted to investigate complete pore clogging from localized precipitation, as well as corresponding changes in permeability and outflow rate. The relations between Fe(II) concentrations and precipitation patterns are further examined to identify the critical zone and threshold Fe(II) concentration. The study provides a comprehensive analysis of how hydrogeochemical reactions—specifically, oxidative precipitation of Fe(II)—affect key physical properties like porosity and permeability of porous medium while bridging

theoretical modeling with real-world challenges in mining (e.g., wells and tailings pond clogging), agriculture (e.g., mineral buildup in irrigation systems), and environmental management (e.g., long-term ASR clogging risks).

2. Mathematical Models for Evolving Pore Space

2.1. Scales to Consider for Hydrogeochemical Processes

Porous mediums in natural and engineered systems exhibit high heterogeneity due to sedimentological processes in the first place but also due to interactions between solid matrix and interstitial fluids. These processes occur across various spatial and temporal scales, including the pore, REV, and continuum scales. The REV is particularly significant, as it balances statistical heterogeneity with localized interactions [36], enabling the development of models that bridge microscale and macroscale processes. However, challenges remain in capturing complex phenomena such as wettability, molecular diffusion, and pore–fluid–solid interactions using single-scale models. To address these limitations, a hybrid-scale approach has been adopted, integrating microscale features, like reactive surface area observed via imaging techniques such as scanning electron microscopy (SEM), into macroscale models. This integration improves the predictive capabilities of porous medium models with the advancement in scientific research and engineering applications [37,38].

Based on these scales of consideration for porous medium processes, this study proposes an integrated numerical method to model the whole pore-clogging phenomena by including the effects of tortuosity on permeability and surface area on reactivity during the Fe(II) oxidative precipitation in a porous medium. Rather than depending on porosity alone, this approach provides a more holistic representation of the complex interactions within porous structures, as well as deeper insights into the spatiotemporal evolution of porous medium under hydrogeochemical circumstances.

2.2. Permeability–Tortuosity–Porosity Model at REV Scale

Mineral precipitation occurs frequently in a reactive environment. The process alters the porosity and flow regime within the porous medium. An emerging method for quantifying changes in fluid flow is to link the evolution of porosity and mineral volume fraction to parameters, e.g., permeability and/or tortuosity, as well as the reactive surface area of minerals.

At the REV scale, porosity is given as the ratio of pore volume to bulk volume. The decrease in porosity could be obtained by taking the volumetric fraction of solid-phase minerals in a REV-scale pore structure. An expression of it can be written as follows:

$$\varnothing = \varnothing_0 - \varphi_i \tag{4}$$

where Φ_0 is the porosity at the initial stage, and φ_i is the mineral volumetric fraction.

Using the mass conservation equation for reactive minerals [39], the temporal evolution of porosity between the current temporal step ($t + \Delta t$) and the former temporal step (t) could be determined as:

$$\varnothing^{t+\Delta t} - \varnothing^t = -\left(\varphi_i^{t+\Delta t} - \varphi_i^t\right) = -V_i S_i k_i f\left(c_j, \mathrm{pH}\right)\Delta t \tag{5}$$

where V_i is the molar volume (L/mol), S_i is the reactive surface area (m^2/L), k_i is the surface-area-normalized rate constant (mol/(m^2·s)), and c_j is the concentration of the solute species (mol/L).

Ferrihydrite (hydrous ferric oxide) is the initial phase formed during Fe(II) oxidative precipitation [40]. Unlike crystalline Fe oxides such as goethite or hematite, ferrihydrite exhibits amorphous, gel-like properties with variable water content and density, making its

molar volume difficult to define. For modeling purposes, we assumed a constant molar volume of 23.99 cm^3/mol for Fe precipitates based on Fe oxide values in the literature [41]. However, ferrihydrite's highly variable molar volume introduces uncertainties in pore-scale predictions, as its occupied volume depends on local environmental conditions (e.g., pH, ionic strength, microbial activity). Addressing this variability is a key focus for future development, with plans to incorporate ferrihydrite's dynamic density and water content into the model.

The flow channel is characterized by a length that exceeds that of a direct pathway connecting the starting and end point [20], so tortuosity can be given as the ratio of the effective traveling length through a flow channel to the straight-line distance between two points. Here, Archie's Law is chosen to illustrate the tortuosity at the following temporal step:

$$\tau^{t+\Delta t} = \left(\varnothing^{t+\Delta t}\right)^{1-m} \tag{6}$$

where m is the cementation exponent. In an earlier study [23], it was experimentally determined to be 7/4 for Fe precipitation in granular materials.

The permeability, as a parameter reflecting the ability of the porous medium to allow the transport of gas or fluids, permeability should also be iteratively updated at the end of each temporal step in accordance with a novel permeability–tortuosity–porosity model [23], which was developed by upscaling the Hagen–Poiseuille equation and incorporating Fe precipitation in the pore matrix:

$$k^{t+\Delta t} = \left(\frac{\tau^t}{\tau^{t+\Delta t}}\right)^2 \left(\frac{\varnothing^{t+\Delta t}}{\varnothing^t}\right)^3 \left(\frac{1-\varnothing^t}{1-\varnothing^{t+\Delta t}}\right)^2 k^t \tag{7}$$

2.3. Surface-Controlled Reaction with a Power Law Model

The reactivity of the porous medium is usually quantified using the surface area. Studies have demonstrated that models assuming the surface area to be constant disagree with the results from laboratory experiments [16,42,43]. This highlights the significance of considering the evolution of the surface area during mineral precipitation.

According to earlier studies [44–46], hydrous Fe oxides tend to distribute and cover the particle surface uniformly, which has been demonstrated by our recent study on oxidative precipitation of Fe(II) in quartz sand [33]. Hence, the most straightforward and adoptable assumption is that Fe precipitates coat solid particles uniformly. Then, Fe precipitation can be described as a surface-controlled reaction using a power law function.

The reactive surface area is computed after completion of each temporal step:

$$S_i^{t+\Delta t} = S_0 \left(\varphi_i^{t+\Delta t}\right)^w \tag{8}$$

where S_0 is a reference surface area (m^2/L), w is a fitting exponent that was suggested to be 1.0 for Fe(OH)$_3$ [25,47,48].

The mathematical model considers abiotic Fe(II) oxidation and precipitation to isolate geochemical mechanisms at the pore scale. However, iron-related bacteria mediate Fe(II) oxidation to Fe(III) [49–51], significantly accelerating precipitation rates and influencing ferrihydrite properties [4,52]. These biologically driven processes lead to precipitates with higher water content, greater heterogeneity, and variable densities compared to abiotic systems. While this study focuses on abiotic precipitation for simplicity, future model extensions will explore biotic–abiotic interactions, particularly for environments dominated by microbial activity [53,54].

3. Hydrogeochemical Model for Addressing Pore Clogging

3.1. Governing Equations for Seepage Flow and Solute Transport

All numerical simulations were performed using *porousMedia4Foam* (downloaded from https://github.com/csoulain/porousMedia4Foam, accessed on 1 July 2023), an open-sourced package to solve multiscale hydrogeochemical interactions (e.g., pore scale, REV scale, and hybrid scale) [24,25]. Our hydrogeochemical model employs a hybrid approach that integrates the pore-scale model with the REV-scale model. This approach requires only REV-scale properties of the porous medium, as well as physio-chemical properties of specified fluid and solute [3]. Furthermore, it effectively captures highly localized heterogeneities with improved accuracy at the pore scale, as demonstrated in studies by Pavuluri et al. [25]. Therefore, it facilitates the modeling of seepage flow and solute transport in areas free of solids and pores in a single system [34], based on the Darcy–Brinkman–Stokes (DBS) equation over a control volume [55]. The governing equations for fluid flow read:

$$\frac{1}{\varnothing}\left[\frac{\partial \rho_f v_f}{\partial t} + \nabla\left(\frac{\rho_f}{\varnothing} v_f v_f\right)\right] = -\nabla p_f + \rho_f g + \nabla\left[\frac{\mu_f}{\varnothing}\left(\nabla v_f + {}^t\nabla_{v_f}\right)\right] - \frac{\mu_f}{k} v_f \tag{9}$$

$$v_f = -\frac{k}{\mu_f}\left(\nabla p_f - \rho_f g\right) \tag{10}$$

$$\nabla v_f = -\frac{\partial \rho_i \varphi_i}{\partial t}\left(\frac{1}{\rho_f} - \frac{1}{\rho_i}\right) \tag{11}$$

where ρ_f is the fluid density (kg/m^3), v_f is the seepage velocity (m/s), μ_f is the fluid viscosity (Pa·s), p_f is the fluid pressure (Pa), ρ_i is the mineral density (kg/m^3), and g is the acceleration of gravity (m/s^2).

Equation (9) is applicable to the domain no matter what is in a REV. In areas with only fluid, Φ equals 1 and the drag force $\frac{\mu_f}{k} v_f$ plays minor role in fluid flow due to less hydraulic energy dissipation induced by viscous friction along particle solid-fluid interfacial area. In areas with both fluids and solids, Φ ranges from 0 to 1, and the drag force is stronger than the inertial and viscous forces, which leads the equation to Darcy's Law. Additionally, if a solid area is characterized by low permeability and low porosity, the velocity approaches zero, which results in a no-slip boundary condition at the interface between fluid and solid.

Furthermore, the governing equation for the solute transport of chemical species with a molar concentration C_j (in mol/L) in a fully saturated porous medium is given as:

$$\frac{\partial\left(\varnothing C_j\right)}{\partial t} = \nabla\left(v_f C_j - \varnothing D_e \nabla C_j\right) + Q_j \tag{12}$$

where Q_j is the source/sink term (mol/(L·s)), and D_e is the effective diffusion coefficient (m^2/s), combining the effects of tortuosity and hydrodynamic dispersion [24,25]. The effective diffusion coefficient can be estimated using a linear dispersion model:

$$D_e = \varnothing^n D_0\left(1 + \frac{d_{ii}}{D_0}\right) \tag{13}$$

where D_0 is the free-phase diffusion coefficient in fluid liquid (m^2/s), n is the exponent of 1/3 as proposed by Millington and Quirk [56], and d_{ii} is the dispersivity tensor as illustrated below:

$$d_{ii} = \alpha_L \frac{v_i^2}{|v|} + \alpha_T \frac{v_j^2}{|v|} \tag{14}$$

where α_L, α_T is the longitudinal and transverse dispersion coefficient (m), v_i, v_j are fluid velocities corresponding to the components of the velocity field v (m/s).

3.2. Model Set-Up, Boundary, and Initial Conditions

A two-dimensional (2-D) water-saturated domain was established with dimensions of 30 mm (width) × 120 mm (height) (Figure 2). To balance computational accuracy with time cost, the volume size for the domain was set to 10 mm, which resulted in a total of 36 REVs to simulate the porous medium. Initially, the domain was completely saturated with DO-rich water under isothermal conditions. In addition, a specified water flux with Fe(II) and DO was applied to the bottom block of the domain. The top block of the domain was set as the water outlet, which connected to the ambient environment (e.g., 1.0 atm and 20 °C). In addition, no-flow boundary conditions were implemented for the right and left boundaries.
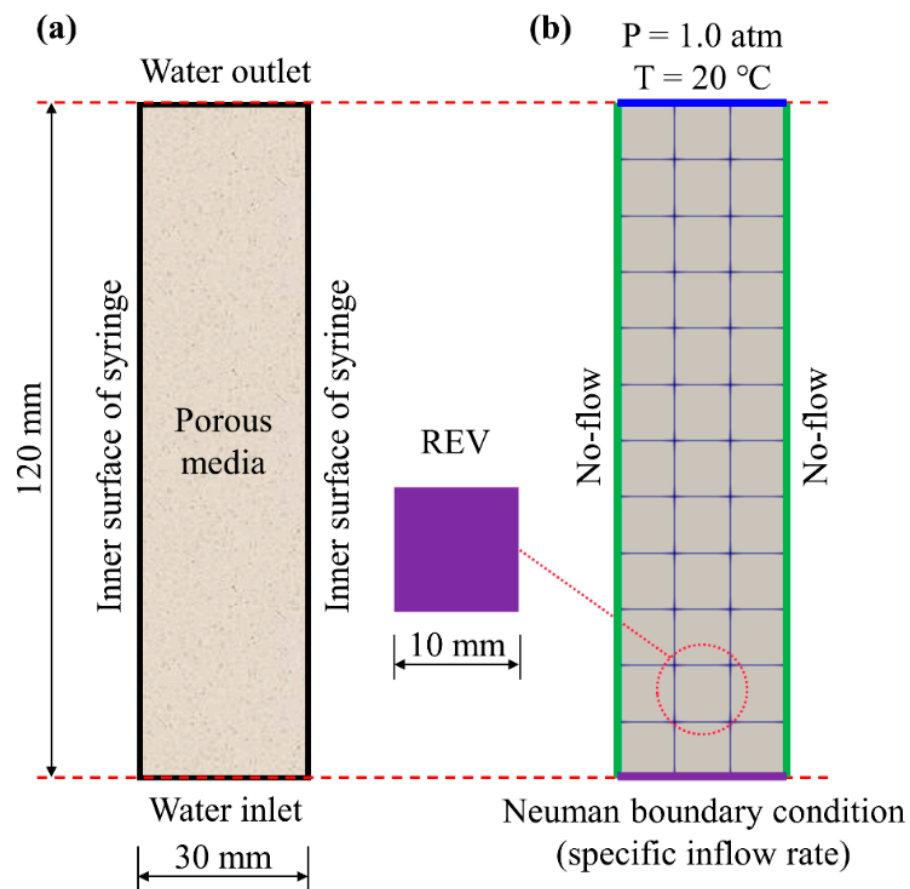

Figure 2. (**a**) The experimental set-up at full scale, and (**b**) Lab-scale numerical simulation set-up, including domain dimensions, REV size, and boundary conditions.

The properties of porous medium and fluids, as well as the injection scheme and reaction rates adopted in the benchmark, are presented in Table 1.

To explore the hydrogeochemical effects on a porous medium due to the mixing of Fe(II)-rich water and DO-rich water, various injection schemes and Fe(II) concentrations are selected. Table 2 outlines all variations in the model parameters for each simulation case. Each case is named in a distinct string format, which enables clear identification and comparison of different parameter combinations in the subsequent analysis.

Table 1. Values of modeling parameters used in the benchmark case.

Category	Description	Value
Soil properties (glass beads)	Dry density, ρ_d (kg/m^3)	1600 [a]
	Initial porosity, Φ_0 (-)	0.35 [a]
	Initial permeability, k_0 (m^2)	7.0×10^{-11} [a]
	Median particle size, d_{50} (mm)	0.83 [a]
Fe(II)-rich water properties	Fe(II) concentration, $C_{Fe(II)}$ (mol/L)	0.001
	Density, ρ_{fw} (kg/m^3)	1000
	pH	4.0 [a]
DO-rich water properties	DO concentration, C_{DO} (mol/L)	2.25×10^{-4} [b]
	Density, ρ_{sw} (kg/m^3)	1025
	pH	8.0 [a]
Injection scheme and transport properties	Inflow rate, q (mL/day)	120
	V_{fw}/V_{ow} (-)	1.0
	Duration, t (d)	15
	Free-phase diffusion coefficient, D_0 (m^2/s)	1.0×10^{-9} [c]
	Longitudinal dispersion coefficient, α_L (m)	1.0×10^{-5} [c]
	Transverse dispersion coefficient, α_T (m)	0
Reaction rates and mineral parameters	Rate constant of Fe oxidation, k_{ox} (L^3/(mol^3·s))	2.46×10^{14} [d]
	Rate constant of Fe precipitation, k_{pr} (mol/(m^2·s))	5.0×10^{-6} [c]
	Mineral density, ρ_s (kg/m^3)	4370 [c]
	Molar volume (L/mol)	0.024 [c]
	Reference surface area, S_0 (m^2/L)	0.001 [c]

Note. [a] Based on laboratory tests [23,33]. [b] 7.2 mg/L equivalents based on oxygen solubility in saltwater of 35 ppt (equivalent to g/kg) at 20 °C. [c] Values given by Xie et al. [41] and verified by Pavuluri et al. [25]. [d] The value converted from a universal rate constant [33].

Table 2. Parameter settings for various simulation cases (Item 1 is the benchmark).

Item	Case ID	Injection Scheme (mL/day)		Hydrochemistry (mmol/L)		Rm
		V_{fw}	V_{ow}	$C_{Fe(II),fw}$	$C_{DO,sw}$	
1	S1_F1	60	60	1	0.225	1:0.225
2	S1_F10	60	60	10	0.225	1:0.023
3	S1_F100	60	60	100	0.225	1:0.002
4	S3_F1	60	180	1	0.225	1:0.675
5	S3_F10 [a]	60	180	10	0.225	1:0.068
6	S3_F100	60	180	100	0.225	1:0.007
7	S9_F1	60	540	1	0.225	1:2.025
8	S9_F10	60	540	10	0.225	1:0.203
9	S9_F100	60	540	100	0.225	1:0.020

Note. [a] S3_F10 represents a combination of V_{fw}/V_{ow} = 1:3, and a Fe(II) concentration of 10 mmol/L. V_{fw} denotes the volume of Fe(II)-rich water, and V_{ow} represents the volume of oxic (DO-rich) water.

Additionally, the molar ratio (*Rm*) of Fe(II)-rich water to DO-rich water is used to investigate the system's hydrochemistry. It is expressed as follows:

$$Rm = \frac{c_{Fe(II)} \cdot V_{fw}}{c_{DO} \cdot V_{ow}} \tag{15}$$

The Fe(II) concentrations used in this study (i.e., 1, 10, and 100 mmol/L) were chosen to simulate high-stress geochemical environments, such as acid mine drainage (AMD) or

industrial sites with elevated Fe(II) loading. While these values exceed the natural concentration (generally below 0.1 mmol/L), they allow us to investigate pore-scale clogging under extreme scenarios. For lower-concentration settings, the model can be adapted by adjusting initial conditions and kinetic parameters to better reflect natural groundwater systems. Based on the variables identified above, a total of 9 simulation cases were performed to investigate the characteristics of precipitation zones and patterns, and the ratio Rm ranges from 1:0.002 to 1:2, which covers a wide spectrum spanning from super anoxic to adequately oxic conditions.

3.3. Spatial and Temporal Discretization

From a numerical perspective, sufficiently small cell size and time step are essential to achieve temporal accuracy and numerical stability. The program utilizes the Courant (Co) criterion to determine the appropriate grid discretization for each cell. It is characterized as:

$$Co = \frac{\Delta t}{\Delta x}\left|v_f\right| < 1.0 \tag{16}$$

where Δt is the temporal step (s), and Δx is the size of cells in the velocity direction (m).

Although velocities may vary across the domain, the simulation must ensure that the Co remains below 1.0 everywhere. In the worst-case scenario, a maximum Co corresponds to the combination of more significant flow velocity and more minor temporal steps. With a fixed cell size (i.e., Δx = 10 mm), the maximum Co occurs near the inlet where the velocity is highest. Thus, the temporal step Δt must be set to be less than or equal to:

$$\Delta t = \frac{Co\Delta x}{\left|v_f\right|} = \frac{1.0 \times 0.01}{2.315 \times 10^{-5}/0.35} = 151\ s \tag{17}$$

In this study, the time step is set to 10 s to guarantee the convergence of chemical reactions, thereby yielding a maximum Co of 0.066 (<1.0 as required) throughout the domain. While the selection of time steps may be relatively arbitrary, it has been demonstrated to ensure mathematical convergence during Fe precipitation in porous mediums.

4. Critical Zone and Numerical Results

4.1. Identification of Critical Zone

While precipitated Fe may accumulate at the bottom of the model domain, the flow can bypass this region without significantly affecting outflow rates. Moreover, approaching pore-clogging could occur near the inlet and lead to a reduction in local porosity and permeability, which consequently elevates the hydraulic gradient between the inlet and outlet. In turn, this can result in a notable increase in the pressure gradient, which facilitates the constant inflow rate in accordance with Darcy's Law. These processes can increase the effective wetting flow path along the flow direction, thereby altering seepage properties (e.g., tortuosity and permeability) and subsequently influencing solute transport and chemical reactions in the porous structure. Hence, it is more important to identify the critical zone characterized by intensive Fe precipitation rather than to quantify the total amount of Fe precipitation in all simulation scenarios.

The results from the spatiotemporal evolution of the volumetric fraction of Fe precipitation in the porous medium indicate that Fe precipitation accumulated progressively near the inlet, with a distinct peak in the volume fraction of Fe(OH)$_3$ (Figure 3). This leads to the identification of a critical zone for precipitation roughly a quarter of the height of the column. While complete pore-clogging is inevitable over time (i.e., the Fe(OH)$_3$ volume fraction increased from 0.08 to 0.35), it may also be influenced by factors such as increased

Fe(II) concentration. Consequently, a simulation duration of 360 days was considered representative, and all subsequent cases were based on the results of this 360-day run unless otherwise specified.
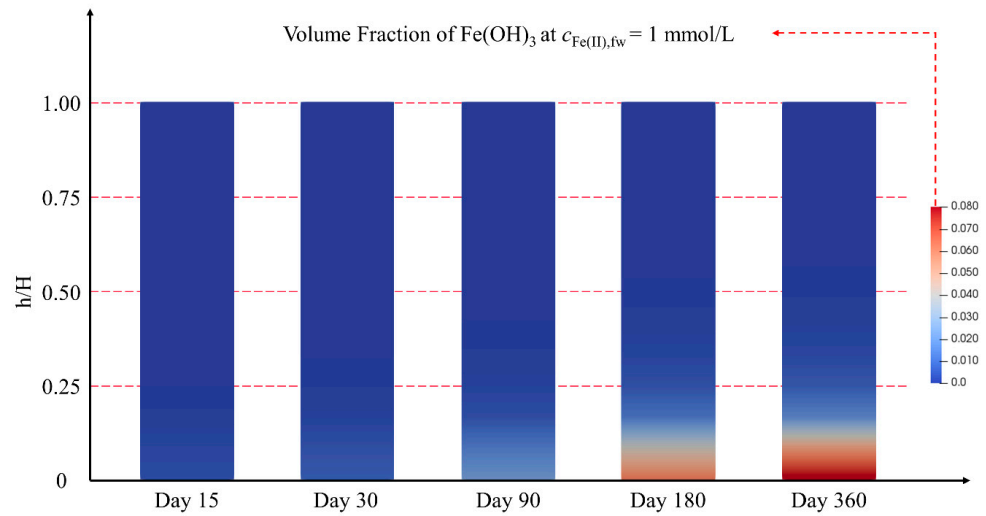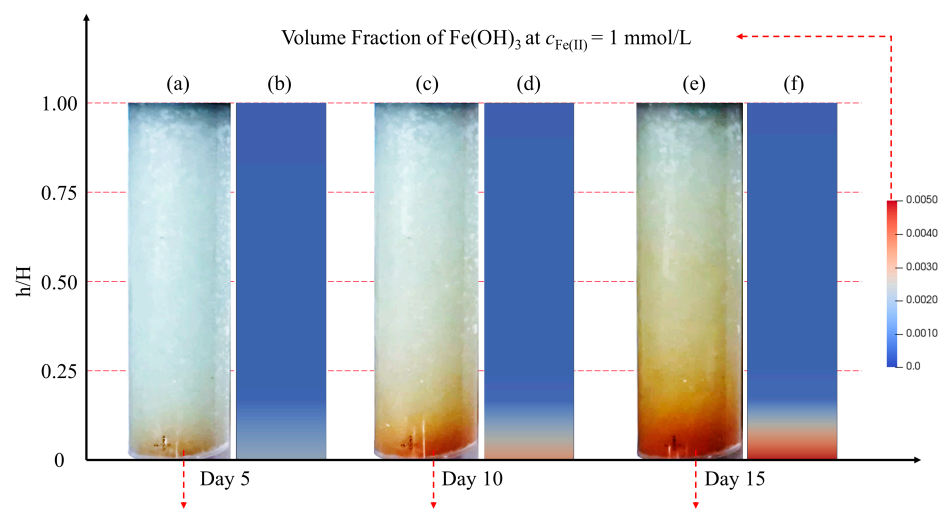

Figure 3. Spatiotemporal evolution of the volume fraction of Fe(OH)$_3$. The contour color represents different volume fractions of Fe precipitation within the porous medium. Note that the value of h/H represents the ratio of a specific height (h, measured from the bottom) to the total height (H).

Model predictions over 15 days were validated against spatiotemporal changes of the critical zone observed in a syringe experiment replicating Fe precipitation driven by mixing of Fe(II)-rich and DO-rich water under conditions in Table 1. The numerical and experimental results showed good agreement (Figure 4), with the precipitation zone expanding vertically to one-fourth of the total height by Day 15. Fe precipitates were estimated at 0.6 g in mass and a volume fraction of 0.14% based on a mineral density of 4370 kg/m^3, consistent with the mean value predicted on Day 15. By including time-dependent changes in tortuosity and surface area (Equations (6) and (8)), the model successfully reproduced the spatial distribution of the critical zone and the Fe precipitate volume fraction, which demonstrated its ability to refine dynamic parameters and simulate mineral precipitation with high accuracy.

The dark coloration represents the area affected by intense Fe(OH)$_3$ rather than the true volume of Fe(OH)$_3$

Figure 4. Temporal evolution of the Fe precipitation zone between experimental results and modeling outcomes. The red regions in (**a,c,e**) indicate areas with intense Fe(OH)$_3$ rather than the actual volume,

while the contour plots in (**b,d,f**) represent different volume fractions of Fe precipitation. Note that the value of h/H represents the ratio of a specific height (h, measured from the bottom) to the total height (H).

4.2. Multiple V_{fw}/V_{ow} with a Constant $C_{Fe(II)}$

To provide an in-depth understanding of the scenarios in Table 2, multiple ratios of V_{fw}/V_{ow} were first explored with a constant Fe(II) concentration (denoted as $C_{Fe(II)}$). Figure 5 presents the simulation results, including the outflow rate over time, volume fraction of Fe(OH)$_3$, and changes in porosity and permeability along the height.
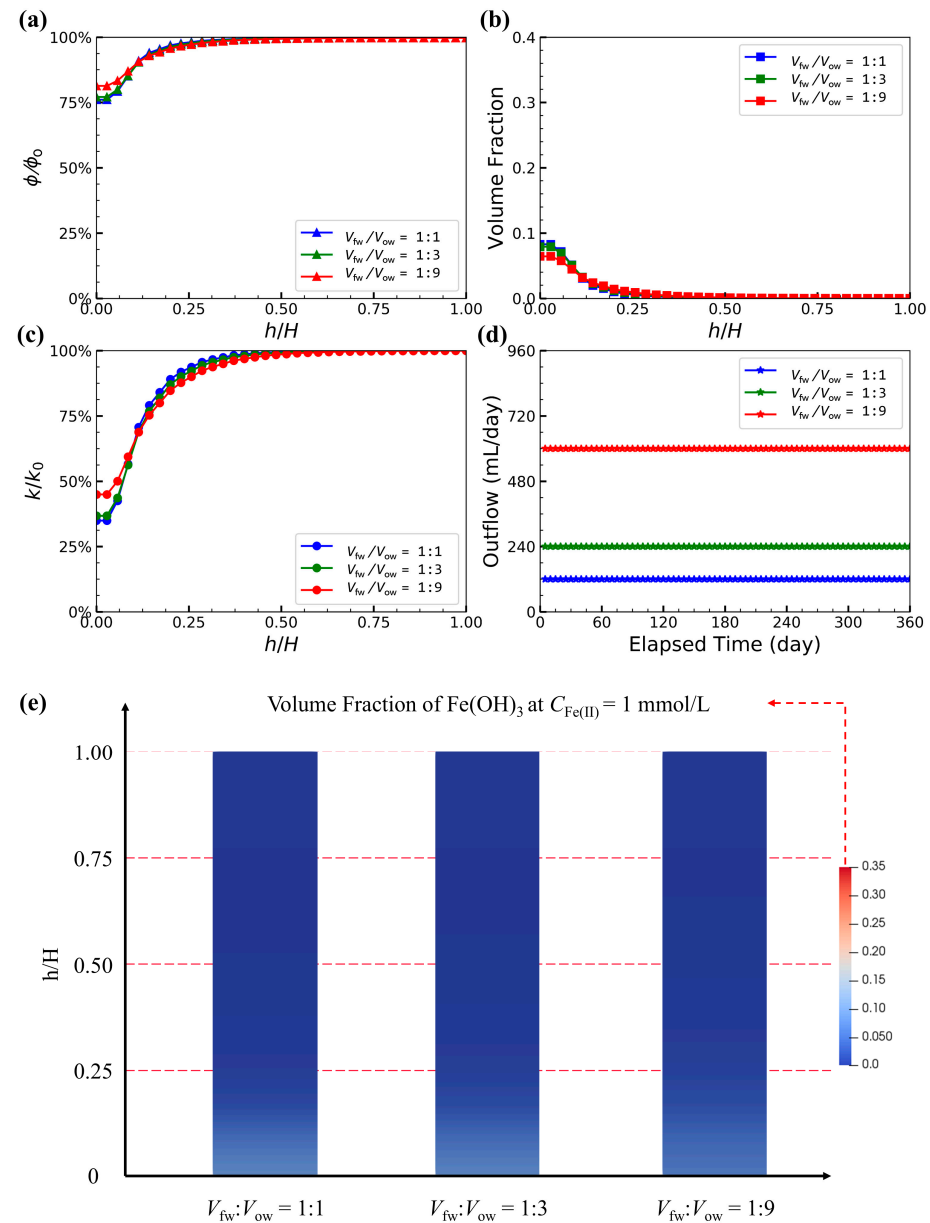

Figure 5. Spatial changes in (**a**) a ratio of the porosity (Φ) to initial porosity (Φ_0), (**b**) volume fraction of Fe(OH)$_3$, (**c**) a ratio of permeability (k) to initial porosity (k_0), (**d**) outflow rate over time, and (**e**) contour plot of volume fraction of Fe(OH)$_3$ under multiple V_{fw}/V_{ow} with a constant $C_{Fe(II)}$. Note that (1) the value of h/H represents the ratio of a specific height (h, measured from the bottom) to the total height (H). (2) the maximum volume fraction is capped at 0.35, which indicates complete pore-clogging.

Figure 5b illustrates a substantial accumulation of Fe precipitation in the critical zone, which resulted in a notable decrease in porosity (up to 25% according to Figure 5a) and permeability (up to 65% according to Figure 5c). Despite these significant alternations near the inlet, the outflow rate remained unaffected (see Figure 5d), which indicated incomplete pore-clogging in 360-day simulation (refer to Figure 5a). Generally, an increase in V_{ow} can enhance the daily supply of DO by increasing the inflow rate, thus promoting the oxidative precipitation of Fe(II). However, minimal variations were observed in terms of changes in porosity and permeability for multiple V_{fw}/V_{ow}. This can be attributed to the dilution effect on dissolved Fe(II) due to the mixing of a constant V_{fw} and increased V_{ow} near the inlet. Specifically, the increase in V_{ow} individually reduced Fe(II) concentration through the mixing, which limited the availability of essential reactants for subsequent reactions with DO. As a result, the oxidative precipitation processes exhibited characteristics similar to the benchmark (i.e., $V_{fw}/V_{ow} = 1$), which presented minor changes in the precipitation zone, as illustrated in Figure 5e.

4.3. Multiple $C_{Fe(II)}$ with a Constant V_{fw}/V_{ow}

In scenarios where groundwater is severely impacted by mine drainage, Fe(II) concentrations can reach exceptionally high levels, ranging from a few mg/L to exceeding 1000 mg/L (equivalent to approximately 20 mmol/L) [57,58]. From a theoretical perspective, elevated $C_{Fe(II)}$ can accelerate the precipitation process and the initiation of pore-clogging in the syringe. To analyze such an extreme case of complete pore-clogging, multiple values of $C_{Fe(II)}$ were investigated while maintaining a constant ratio of V_{fw}/V_{ow}. Figure 6 illustrates the simulation results, including the outflow rate over time, volume fraction of Fe(OH)$_3$, and changes in porosity and permeability along the height.

Three key findings can be drawn from Figure 6. First, compared to the benchmark with $C_{Fe(II)} = 1$ mmol/L, higher Fe(II) (i.e., 10 mmol/L and 100 mmol/L) led to more rapid precipitation and thus accelerated pore-clogging process in the critical zone (see Figure 6e). Second, while pore-clogging occurred at both $C_{Fe(II)} = 10$ mmol/L (refer to green lines in Figure 6a–c) and $C_{Fe(II)} = 100$ mmol/L (refer to red lines in Figure 6a–c), distinct precipitation patterns exhibited in the critical zone. At $C_{Fe(II)} = 10$ mmol/L, clogging was confined to a narrow region near the inlet (green line in Figure 6b), whereas, at $C_{Fe(II)} = 100$ mmol/L, the entire critical zone (i.e., one-quarter of the total height) became clogged with Fe(OH)$_3$ precipitates (red line in Figure 6b; dark red in Figure 6e), which resulted in zero permeability across this region (red lines in Figure 6c). Third, approaching pore-clogging at $C_{Fe(II)} = 10$ mmol/L had no impact on the outflow rate, but at $C_{Fe(II)} = 100$ mmol/L, a notable reduction in outflow rate was observed after 260 days (red line in Figure 6d), which dropped to 100 mL/day by Day 320 when the simulation was terminated. This is consistent with the formation of a geochemical barrier. These findings suggest that the pore-clogging zone must be sufficiently wide to affect outflow and alter the fluid field; otherwise, the flow will remain constant according to boundary conditions. In summary, $C_{Fe(II)}$ not only controls the heterogeneous distribution of Fe precipitation but also dictates flow patterns through localized pore-clogging.

The results reflect Fe(II) concentrations characteristic of geochemical environments (e.g., AMD systems) where low pH and elevated Fe(II) levels accelerate Fe(II) oxidation and precipitation. While this approach captures extreme pore-clogging, it may overestimate clogging rates in natural systems with lower Fe(II) concentrations. For typical groundwater conditions (<1 mmol/L or 55.8 mg/L), slower reaction rates and precipitation dynamics would require modified input parameters. Future work could include pH dependence to extend the model to environmentally realistic Fe(II) concentrations observed in natural groundwaters.
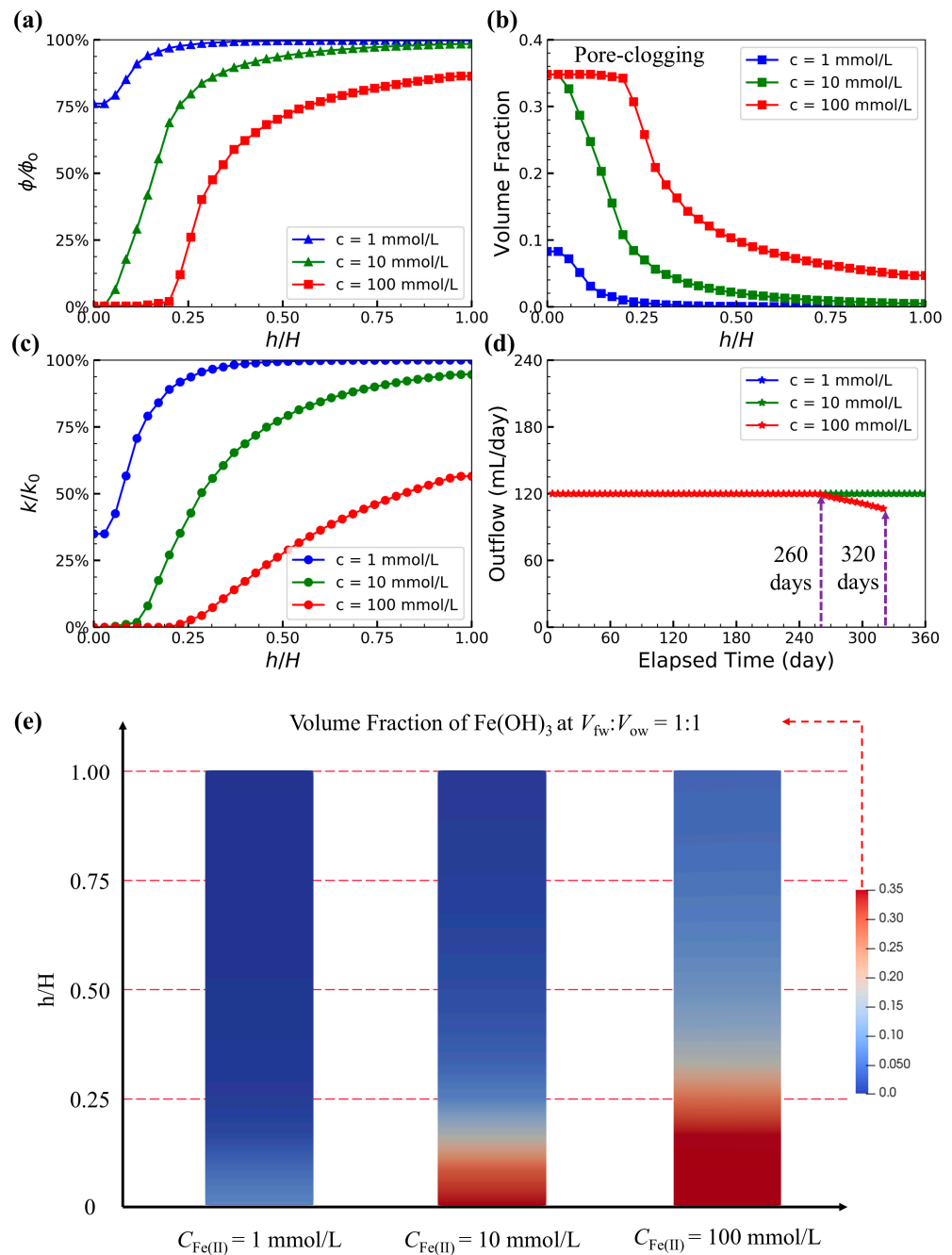
Figure 6. Spatial changes in (**a**) a ratio of the porosity (Φ) to initial porosity (Φ_0), (**b**) volume fraction of Fe(OH)$_3$, (**c**) a ratio of permeability (k) to initial porosity (k_0), (**d**) outflow rate over time, and (**e**) contour plot of volume fraction of Fe(OH)$_3$ under multiple $C_{Fe(II)}$ with a constant V_{fw}/V_{ow}. Note that (1) the value of h/H represents the ratio of a specific height (h, measured from the bottom) to the total height (H). (2) the maximum volume fraction is capped at 0.35, which indicates complete pore-clogging.

4.4. Effect of Rm Ratio on Precipitation Patterns

Figure 7 illustrates the precipitation patterns for different values of Rm, which covers a wide range from highly anoxic (left) to adequately oxic (right) conditions. A general trend was observed that the height of the precipitation zone decreased as Rm increased from 1:0.002 to 1:2.025. Under more anoxic conditions (lower Rm), the precipitation zone became more dispersed with a broader spatial distribution. This is attributed to the higher availability of $C_{Fe(II)}$, which promoted reactive transport of Fe(II) throughout the height and consequently led to the precipitation of Fe(OH)$_3$ over a larger area. In contrast, under more

oxic conditions (higher Rm), the precipitation zone is more concentrated near the inlet. This is primarily due to the reduced availability of $C_{Fe(II)}$, which restricts the expansion of the precipitation zone.
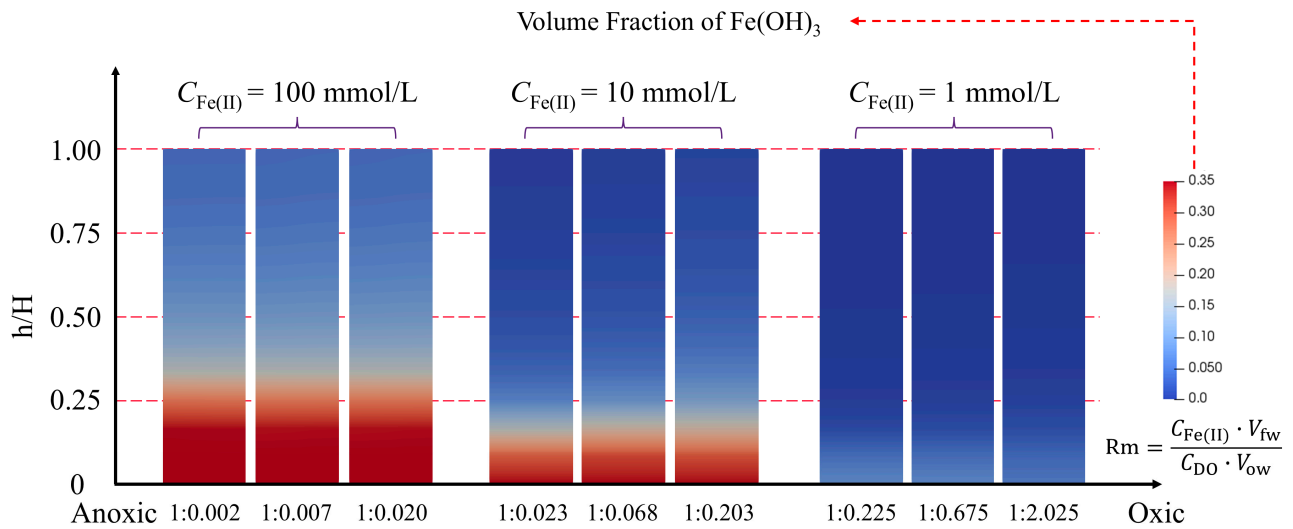

Figure 7. Spatial changes in volume fraction of Fe(OH)$_3$ for different Rm. Note that the maximum volume fraction is capped at 0.35, which indicates complete pore-clogging.

Furthermore, the results show that complete pore-clogging initiated at a critical Fe(II) concentration, which, for this study's time scale of 360 days, corresponds to a maximum volume fraction of 0.35. As $C_{Fe(II)}$ increases, hydrogeochemical reactions are accelerated, and more rapid pore-clogging occurs. However, this process may become limited by insufficient DO. In contrast, when $C_{Fe(II)}$ was lower (i.e., 1 mmol/L) but DO was adequate, Fe(II) was swiftly depleted before it could be transported to higher regions, which resulted in a less distinct precipitation zone localized near the inlet. These factors create a localized zone of intensive Fe precipitation, which significantly alters the seepage properties of a porous medium. Over time, this zone acts as a geochemical barrier, slowing groundwater flow and solute transport, thereby influencing the overall behavior of hydrogeological systems.

Note that the results presented are based on the molar volume simplification for the precipitating Fe. While this simplifies the modeling process, it likely underestimates variability in permeability and porosity evolution caused by ferrihydrite's gel-like nature, which undergoes density and volume changes over time. Future research should adopt a more dynamic approach, incorporating variable water content and recrystallization kinetics for more accurate predictions.

5. Discussion and Implication

5.1. Dynamic Properties of Ferrihydrite

Our physio-mathematical model employs static physical properties for ferrihydrite (e.g., density, molar volume), which may introduce some uncertainties for modeling. Ferrihydrite, an amorphous Fe hydroxide and an initial precipitate in geochemical systems [1], gradually recrystallizes into more stable phases such as goethite or hematite [59]. This transformation reduces pore volume due to densification, decreases surface area, affects reaction kinetics, and increases density while lowering water content [60]. These dynamic changes present challenges for modeling ferrihydrite's behavior at pore and hybrid scales. While the transformation was not included in the study, future iterations of the model will seek to incorporate time-dependent changes in ferrihydrite's density, volume, and surface area, as well as their effects on pore-scale processes. Coupling the permeability–

tortuosity–porosity model with geochemical simulators (e.g., TOUGHREACT) [61] will enable a more dynamic representation. Additionally, experimental studies on ferrihydrite's transformation and density under varying conditions will provide significant validation data and enhance the model's ability to represent permeability and porosity evolution over long timescales.

5.2. Microbial Activity on Fe(III) Precipitation

To isolate the geochemical mechanisms of pore-scale precipitation, the model simplifies Fe(II) oxidation only driven by DO availability, and the results presented reflect abiotic Fe(III) precipitation dynamics. In contrast, biological processes, particularly bacterial mediation, play an important role in Fe(II) oxidation and precipitation under natural conditions [4,50]. In aerobic environments, Fe-oxidizing bacteria can enhance the oxidation of Fe(II) to Fe(III) and promote faster precipitation of Fe oxides [52,62]. These processes, coupled with interaction with a variety of organic matter and inorganic compounds [63,64], introduce additional complexity by accelerating precipitation rates, reducing porosity more rapidly, and increasing greater heterogeneity in precipitate distribution. In addition, extracellular polymeric substances produced by Fe-related bacteria can trap water and reduce precipitate density, altering the permeability of the system [65]. These factors highlight the need to incorporate microbial activity into the model to capture the coupled effects of biotic and abiotic processes. Further research aims to integrate microbial facilitation using experimental validation and numerical platforms that couple these mechanisms. This advancement will enhance the model's applicability to mineral precipitation in environments where microbial activity is prevalent.

5.3. Auto-Catalytic Feedback Mechanism

The injection of Fe(II)-rich water into a background of DO-rich water results in the oxidation of Fe(II) to Fe(III), precipitating as Fe oxides (e.g., $Fe(OH)_3$) along the flow path, with a peak in $Fe(OH)_3$ volume fraction near the inlet. This process reduces permeability and porosity at the bottom of the model domain, consistent with the hypothesis of a critical zone influenced by DO availability. In natural systems, the auto-catalytic nature of Fe(III) precipitation significantly affects porosity and permeability heterogeneity. Early-stage precipitates, such as ferrihydrite, act as catalytic surfaces that enhance further oxidation of Fe(II), leading to localized zones of intense precipitation [66]. This self-sustaining process promotes preferential growth on pre-existing surfaces, exacerbating pore clogging in certain regions while leaving others relatively unaffected. Such feedback mechanisms accelerate permeability reduction in specific flow channels, consistent with the modeled changes in porosity and permeability (Figure 6a,c). Compared to the surface-controlled reaction using a power-law function (Equation (8)), previous studies have proposed exponential models to describe how earlier minerals influence the reactivity of later minerals [14,67]. It would be interesting to compare these models and incorporate auto-catalytic feedback in our future research.

5.4. Scalability and Field-Scale Implications

Fe oxides, represented as $Fe(OH)_3$ in its chemical formula, are selected for this study due to their significance in environmental systems characterized by high Fe(II) fluxes, such as industrial discharge sites. However, ferrihydrite's gel-like nature and its transformation introduce complexities and challenges in the direct application of the modeling approach, for instance, high variability in density and molar volume due to water content and transformation into crystalline forms (e.g., goethite, hematite) over time. By assuming static physical properties for ferrihydrite (e.g., density, molar volume) and introducing time-dependent tortuosity and surface-controlled reactivity, this study provides a theoretical framework

for modeling the coupled evolution of porosity and permeability during Fe precipitation in porous medium. While the inherent complexities of ferrihydrite limit its immediate applicability, the model is applied to Fe oxides due to their environmental importance. To enhance practical utility, future studies will extend the permeability–tortuosity–porosity model to simpler mineral systems, such as barite ($BaSO_4$) and calcite ($CaCO_3$), which exhibit predictable precipitation behaviors and avoid the uncertainties of ferrihydrite. These extensions will improve the model's generality and facilitate its applications across diverse hydrogeochemical systems. Furthermore, collaboration with experienced geochemists will further address the complexity of ferrihydrite. Such interdisciplinary efforts will enhance the model's ability to accurately simulate mineral precipitation and its impact on pore-scale processes.

While this study focuses on a theoretical model and benchmark simulations, a syringe experiment involving Fe(II) precipitation under controlled conditions provided valuable data on spatial heterogeneity, which established the credibility of predictive models for the porous medium. Nevertheless, the experimental phenomena may be influenced by factors such as microbial mediation and flow path heterogeneities, which are not included in the current model. Also, pore volume reduction and corresponding constraints on fluid flow have not been qualitatively compared with published studies. To better capture the dynamic coupling between geochemical reactions and pore-scale transport processes, future efforts will involve advanced experiments or leveraging existing datasets to validate thresholds for complete pore clogging. Specifically, column studies simulating Fe(II) precipitation under varying flow and concentration conditions will generate quantitative data to refine the permeability–tortuosity–porosity model. Collaborations on imaging techniques, such as micro-CT or SEM, will further validate spatial precipitation patterns predicted by the novel model.

Scaling hybrid-scale model findings to field-scale applications requires addressing spatial and temporal heterogeneity in flow and geochemical conditions. In field settings, localized precipitation patterns, influenced by hydrodynamic dispersion and variable Fe(II) fluxes, can create anisotropic porosity and permeability changes [39,68]. Field-scale implementation also involves coupling the permeability–tortuosity–porosity model with large-scale reactive transport frameworks, such as MODFLOW, FLOTRAN, or TOUGHRE-ACT [3,41], to simulate regional hydrogeochemical impacts. For instance, in AMD remediation, the model could predict well the clogging rates under varying Fe(II) inputs, enabling regional-scale forecasts of permeability evolution and mineral precipitation patterns. Such predictions can support engineering solutions for groundwater management and sustainable remediation in hydrogeological systems.

6. Conclusions

The Fe(II) oxidative precipitation significantly impacts the seepage properties—porosity, permeability, and tortuosity—of a porous medium. These long-term changes are critical for the functioning of hydrogeological systems, as they affect groundwater flow, solute transport, and geochemical reactions. To analyze the increasing complexity of pore-clogging caused by Fe precipitation, a hybrid-scale reactive transport package (*porousMedia4Foam* coupling OpenFOAM and PHREEQC) was utilized. This approach allows us to benchmark the numerical implementation of the permeability–tortuosity–porosity relationship and assess the feedback of surface-controlled reactions, particularly the potential for complete clogging in the pore matrix due to mineral precipitation.

Based on benchmark simulations and parametric analyses, the study makes the following major contributions:

(1) A physio-mathematical model was developed to integrate the effects of tortuosity on permeability and surface area impacts on reactivity during oxidative precipitation of Fe(II). This extends the KC equation and provides a framework for addressing pore-clogging phenomena.

(2) A process-based numerical model was established using a hybrid-scale approach, Which revealed patterns of Fe precipitation identified as critical zones for pore clogging.

(3) The ratio of $V_{\mathrm{fw}}/V_{\mathrm{ow}}$ had minimal influence on precipitation patterns, while Fe(II) concentration significantly affected the distribution of Fe precipitation, regulating flow patterns through localized clogging.

(4) A critical Fe concentration of 10 mmol/L was identified as a threshold: beyond this level, clogging accelerates significantly over time in the porous medium.

(5) The permeability–tortuosity–porosity relationship was extensively validated through simulations, confirming its applicability for addressing pore-clogging challenges in hydrogeological systems.

In conclusion, this study represents a significant advancement in modeling hydrogeo-chemical processes in granular soils with Fe precipitation. The integrated model provides insights into the temporal evolution of pore matrices and offers practical applications in mining (e.g., mine drainage), agriculture (e.g., groundwater wells), and environmental management (e.g., soil remediation). This framework can be incorporated into regional engineering-scale models to better simulate in situ conditions, bridging the gap between theoretical understanding and practical application.

References

1. Cornell, R.; Schwertmann, U. *The Iron Oxides: Structure, Properties, Reactions, Occurrences and Uses*; Wiley-VCH Verlag GmbH & Co. KGaA: Weinheim, Germany, 2003; ISBN 978-3-527-30274-1.

2. Larrahondo, J.M.; Burns, S.E. Laboratory-Prepared Iron Oxide Coatings on Sands: Surface Characterization and Strength Parameters. *J. Geotech. Geoenviron. Eng.* **2014**, *140*, 04013052. [CrossRef]

3. Cao, W.; Yan, G.; Hofmann, H.; Scheuermann, A. State of the Art on Fe Precipitation in Porous Media: Hydrogeochemical Processes and Evolving Parameters. *J. Mar. Sci. Eng.* **2024**, *12*, 690. [CrossRef]

4. Cao, W.; Hofmann, H.; Yan, G.; Scheuermann, A. Porewater Exchange and Iron Transformation in a Coastal Groundwater System: A Field Investigation, Driving Mechanisms Analysis, and Conceptual Model. *Front. Mar. Sci.—Sec Coast. Ocean Process.* **2024**, *11*, 1385517. [CrossRef]

5. Tenthorey, E.; Fitzgerald, J. Feedbacks between Deformation, Hydrothermal Reaction and Permeability Evolution in the Crust: Experimental Insights. *Earth Planet. Sci. Lett.* **2006**, *247*, 117–129. [CrossRef]

6.　Annandale, J. Modelling the Long-Term Effect of Irrigation with Gypsiferous Water on Soil and Water Resources. *Agric. Ecosyst. Environ.* **1999**, *76*, 109–119. [CrossRef]

7.　Rinck-Pfeiffer, S. Interrelationships between Biological, Chemical, and Physical Processes as an Analog to Clogging in Aquifer Storage and Recovery (ASR) Wells. *Water Res.* **2000**, *34*, 2110–2118. [CrossRef]

8.　Xie, M.; Kolditz, O.; Moog, H.C. A Geochemical Transport Model for Thermo-hydro-chemical (THC) Coupled Processes with Saline Water. *Water Resour. Res.* **2011**, *47*, 2010WR009270. [CrossRef]

9.　Liu, S.; Jacques, D.; Govaerts, J.; Wang, L. Conceptual Model Analysis of Interaction at a Concrete–Boom Clay Interface. *Phys. Chem. Earth Parts ABC* **2014**, *70–71*, 150–159. [CrossRef]

10.　Houben, G.J. Iron Oxide Incrustations in Wells. Part 1: Genesis, Mineralogy and Geochemistry. *Appl. Geochem.* **2003**, *18*, 927–939. [CrossRef]

11.　Wagner, R.; Kühn, M.; Meyn, V.; Pape, H.; Vath, U.; Clauser, C. Numerical Simulation of Pore Space Clogging in Geothermal Reservoirs by Precipitation of Anhydrite. *Int. J. Rock Mech. Min. Sci.* **2005**, *42*, 1070–1081. [CrossRef]

12.　Rassi, E.M.; Codd, S.L.; Seymour, J.D. Nuclear Magnetic Resonance Characterization of the Stationary Dynamics of Partially Saturated Media during Steady-State Infiltration Flow. *New J. Phys.* **2011**, *13*, 015007. [CrossRef]

13.　De Windt, L.; Pellegrini, D.; Van Der Lee, J. Coupled Modeling of Cement/Claystone Interactions and Radionuclide Migration. *J. Contam. Hydrol.* **2004**, *68*, 165–182. [CrossRef] [PubMed]

14.　Seigneur, N.; Mayer, K.U.; Steefel, C.I. Reactive Transport in Evolving Porous Media. *Rev. Mineral. Geochem.* **2019**, *85*, 197–238. [CrossRef]

15.　Jin, L.; Mathur, R.; Rother, G.; Cole, D.; Bazilevskaya, E.; Williams, J.; Carone, A.; Brantley, S. Evolution of Porosity and Geochemistry in Marcellus Formation Black Shale during Weathering. *Chem. Geol.* **2013**, *356*, 50–63. [CrossRef]

16.　Sabo, M.S.; Beckingham, L.E. Porosity-Permeability Evolution During Simultaneous Mineral Dissolution and Precipitation. *Water Resour. Res.* **2021**, *57*, e2020WR029072. [CrossRef]

17.　Koponen, A.; Kataja, M.; Timonen, J. Permeability and Effective Porosity of Porous Media. *Phys. Rev. E* **1997**, *56*, 3319–3325. [CrossRef]

18.　Hommel, J.; Coltman, E.; Class, H. Porosity–Permeability Relations for Evolving Pore Space: A Review with a Focus on (Bio-)Geochemically Altered Porous Media. *Transp. Porous Media* **2018**, *124*, 589–629. [CrossRef]

19.　Lai, P.; Krevor, S. Pore Scale Heterogeneity in the Mineral Distribution and Surface Area of Berea Sandstone. *Energy Procedia* **2014**, *63*, 3582–3588. [CrossRef]

20.　Ehsan Samaei, S.; Berardi, U.; Taban, E.; Soltani, P.; Mohammad Mousavi, S. Natural Fibro-Granular Composite as a Novel Sustainable Sound-Absorbing Material. *Appl. Acoust.* **2021**, *181*, 108157. [CrossRef]

21.　Werth, C.J.; Zhang, C.; Brusseau, M.L.; Oostrom, M.; Baumann, T. A Review of Non-Invasive Imaging Methods and Applications in Contaminant Hydrogeology Research. *J. Contam. Hydrol.* **2010**, *113*, 1–24. [CrossRef]

22.　Blunt, M.J.; Bijeljic, B.; Dong, H.; Gharbi, O.; Iglauer, S.; Mostaghimi, P.; Paluszny, A.; Pentland, C. Pore-Scale Imaging and Modelling. *Adv. Water Resour.* **2013**, *51*, 197–216. [CrossRef]

23.　Cao, W.; Hu, N.; Yan, G.; Hofmann, H.; Scheuermann, A. Permeability–Porosity Model Considering Oxidative Precipitation of Fe(II) in Granular Porous Media. *J. Hydrol.* **2024**, *636*, 131346. [CrossRef]

24.　Soulaine, C.; Pavuluri, S.; Claret, F.; Tournassat, C. porousMedia4Foam: Multi-Scale Open-Source Platform for Hydro-Geochemical Simulations with OpenFOAM®. *Environ. Model. Softw.* **2021**, *145*, 105199. [CrossRef]

25.　Pavuluri, S.; Tournassat, C.; Claret, F.; Soulaine, C. Reactive Transport Modeling with a Coupled OpenFOAM®-PHREEQC Platform. *Transp. Porous Media* **2022**, *145*, 475–504. [CrossRef]

26.　Kang, Q.; Tsimpanogiannis, I.N.; Zhang, D.; Lichtner, P.C. Numerical Modeling of Pore-Scale Phenomena during CO_2 Sequestration in Oceanic Sediments. *Fuel Process. Technol.* **2005**, *86*, 1647–1665. [CrossRef]

27.　Chagneau, A.; Claret, F.; Enzmann, F.; Kersten, M.; Heck, S.; Madé, B.; Schäfer, T. Mineral Precipitation-Induced Porosity Reduction and Its Effect on Transport Parameters in Diffusion-Controlled Porous Media. *Geochem. Trans.* **2015**, *16*, 13. [CrossRef]

28.　Rajyaguru, A.; L'Hôpital, E.; Savoye, S.; Wittebroodt, C.; Bildstein, O.; Arnoux, P.; Detilleux, V.; Fatnassi, I.; Gouze, P.; Lagneau, V. Experimental Characterization of Coupled Diffusion Reaction Mechanisms in Low Permeability Chalk. *Chem. Geol.* **2019**, *503*, 29–39. [CrossRef]

29.　Fox, D.T.; Guo, L.; Fujita, Y.; Huang, H.; Redden, G. Experimental and Numerical Analysis of Parallel Reactant Flow and Transverse Mixing with Mineral Precipitation in Homogeneous and Heterogeneous Porous Media. *Transp. Porous Media* **2016**, *111*, 605–626. [CrossRef]

30.　Garcia-Rios, M.; Luquot, L.; Soler, J.M.; Cama, J. The Role of Mineral Heterogeneity on the Hydrogeochemical Response of Two Fractured Reservoir Rocks in Contact with Dissolved CO_2. *Appl. Geochem.* **2017**, *84*, 202–217. [CrossRef]

31.　Jung, H.; Navarre-Sitchler, A. Physical Heterogeneity Control on Effective Mineral Dissolution Rates. *Geochim. Cosmochim. Acta* **2018**, *227*, 246–263. [CrossRef]

32. Liu, J.; Aruguete, D.M.; Jinschek, J.R.; Donald Rimstidt, J.; Hochella, M.F. The Non-Oxidative Dissolution of Galena Nanocrystals: Insights into Mineral Dissolution Rates as a Function of Grain Size, Shape, and Aggregation State. *Geochim. Cosmochim. Acta* **2008**, *72*, 5984–5996. [CrossRef]

33. Zhao, Z.; Zhang, C.; Cao, W.; Hofmann, H.; Wang, T.; Li, L. Oxidative Precipitation of Fe(II) in Porous Media: Laboratory Experiment and Numerical Simulation. *ACS EST Water* **2023**, *3*, 963–973. [CrossRef]

34. Soulaine, C.; Tchelepi, H.A. Micro-Continuum Approach for Pore-Scale Simulation of Subsurface Processes. *Transp. Porous Media* **2016**, *113*, 431–456. [CrossRef]

35. Saripalli, K.P.; Serne, R.J.; Meyer, P.D.; McGrail, B.P. Prediction of Diffusion Coefficients in Porous Media Using Tortuosity Factors Based on Interfacial Areas. *Groundwater* **2002**, *40*, 346–352. [CrossRef]

36. Bear, J. *Dynamics of Fluids in Porous Media*; American Elsevier Publishing Company: New York, NY, USA, 1972.

37. Scheibe, T.D.; Perkins, W.A.; Richmond, M.C.; McKinley, M.I.; Romero-Gomez, P.D.J.; Oostrom, M.; Wietsma, T.W.; Serkowski, J.A.; Zachara, J.M. Pore-Scale and Multiscale Numerical Simulation of Flow and Transport in a Laboratory-Scale Column. *Water Resour. Res.* **2015**, *51*, 1023–1035. [CrossRef]

38. Soulaine, C.; Creux, P.; Tchelepi, H.A. Micro-Continuum Framework for Pore-Scale Multiphase Fluid Transport in Shale Formations. *Transp. Porous Media* **2019**, *127*, 85–112. [CrossRef]

39. Steefel, C.I.; Appelo, C.A.J.; Arora, B.; Jacques, D.; Kalbacher, T.; Kolditz, O.; Lagneau, V.; Lichtner, P.C.; Mayer, K.U.; Meeussen, J.C.L.; et al. Reactive Transport Codes for Subsurface Environmental Simulation. *Comput. Geosci.* **2015**, *19*, 445–478. [CrossRef]

40. Zhu, M.; Frandsen, C.; Wallace, A.F.; Legg, B.; Khalid, S.; Zhang, H.; Mørup, S.; Banfield, J.F.; Waychunas, G.A. Precipitation Pathways for Ferrihydrite Formation in Acidic Solutions. *Geochim. Cosmochim. Acta* **2016**, *172*, 247–264. [CrossRef]

41. Xie, M.; Mayer, K.U.; Claret, F.; Alt-Epping, P.; Jacques, D.; Steefel, C.; Chiaberge, C.; Simunek, J. Implementation and Evaluation of Permeability-Porosity and Tortuosity-Porosity Relationships Linked to Mineral Dissolution-Precipitation. *Comput. Geosci.* **2015**, *19*, 655–671. [CrossRef]

42. Noiriel, C. Resolving Time-Dependent Evolution of Pore-Scale Structure, Permeability and Reactivity Using X-Ray Microtomography. *Rev. Mineral. Geochem.* **2015**, *80*, 247–285. [CrossRef]

43. Beckingham, L.E.; Steefel, C.I.; Swift, A.M.; Voltolini, M.; Yang, L.; Anovitz, L.M.; Sheets, J.M.; Cole, D.R.; Kneafsey, T.J.; Mitnick, E.H.; et al. Evaluation of Accessible Mineral Surface Areas for Improved Prediction of Mineral Reaction Rates in Porous Media. *Geochim. Cosmochim. Acta* **2017**, *205*, 31–49. [CrossRef]

44. Auffan, M.; Rose, J.; Bottero, J.-Y.; Lowry, G.V.; Jolivet, J.-P.; Wiesner, M.R. Towards a Definition of Inorganic Nanoparticles from an Environmental, Health and Safety Perspective. *Nat. Nanotechnol.* **2009**, *4*, 634–641. [CrossRef]

45. Hu, Y.; Lee, B.; Bell, C.; Jun, Y.-S. Environmentally Abundant Anions Influence the Nucleation, Growth, Ostwald Ripening, and Aggregation of Hydrous Fe(III) Oxides. *Langmuir* **2012**, *28*, 7737–7746. [CrossRef] [PubMed]

46. Xu, Y.; Axe, L. Synthesis and Characterization of Iron Oxide-Coated Silica and Its Effect on Metal Adsorption. *J. Colloid Interface Sci.* **2005**, *282*, 11–19. [CrossRef]

47. Andreani, M.; Luquot, L.; Gouze, P.; Godard, M.; Hoisé, E.; Gibert, B. Experimental Study of Carbon Sequestration Reactions Controlled by the Percolation of CO_2-Rich Brine through Peridotites. *Environ. Sci. Technol.* **2009**, *43*, 1226–1231. [CrossRef] [PubMed]

48. Luhmann, A.J.; Kong, X.-Z.; Tutolo, B.M.; Garapati, N.; Bagley, B.C.; Saar, M.O.; Seyfried, W.E. Experimental Dissolution of Dolomite by CO_2-Charged Brine at 100 °C and 150 bar: Evolution of Porosity, Permeability, and Reactive Surface Area. *Chem. Geol.* **2014**, *380*, 145–160. [CrossRef]

49. Alotaibi, M.D.; Patterson, B.M.; McKinley, A.J.; Reeder, A.Y.; Furness, A.J.; Donn, M.J. Fate of Benzotriazole and 5-Methylbenzotriazole in Recycled Water Recharged into an Anaerobic Aquifer: Column Studies. *Water Res.* **2015**, *70*, 184–195. [CrossRef]

50. Wu, Z.; Wang, S.; Ji, N. Distribution Character of Localized Iron Microniche in Lake Sediment Microzone Revealed by Chemical Image. *Environ. Sci. Pollut. Res.* **2019**, *26*, 35704–35716. [CrossRef] [PubMed]

51. Luef, B.; Fakra, S.C.; Csencsits, R.; Wrighton, K.C.; Williams, K.H.; Wilkins, M.J.; Downing, K.H.; Long, P.E.; Comolli, L.R.; Banfield, J.F. Iron-Reducing Bacteria Accumulate Ferric Oxyhydroxide Nanoparticle Aggregates That May Support Planktonic Growth. *ISME J.* **2013**, *7*, 338–350. [CrossRef]

52. Baker, I.R.; Matzen, S.L.; Schuler, C.J.; Toner, B.M.; Girguis, P.R. Aerobic Iron-Oxidizing Bacteria Secrete Metabolites That Markedly Impede Abiotic Iron Oxidation. *Proc. Natl. Acad. Sci. Nexus* **2023**, *2*, pgad421. [CrossRef] [PubMed]

53. Spiteri, C.; Slomp, C.P.; Tuncay, K.; Meile, C. Modeling Biogeochemical Processes in Subterranean Estuaries: Effect of Flow Dynamics and Redox Conditions on Submarine Groundwater Discharge of Nutrients: Biochemistry of Subterranean Estuaries. *Water Resour. Res.* **2008**, *44*, W02430. [CrossRef]

54. McAllister, S.M.; Barnett, J.M.; Heiss, J.W.; Findlay, A.J.; MacDonald, D.J.; Dow, C.L.; Luther, G.W.; Michael, H.A.; Chan, C.S. Dynamic Hydrologic and Biogeochemical Processes Drive Microbially Enhanced Iron and Sulfur Cycling within the Intertidal Mixing Zone of a Beach Aquifer: Fe and S Cycling in a Beach Aquifer. *Limnol. Oceanogr.* **2015**, *60*, 329–345. [CrossRef]

55. Pavuluri, S.; Maes, J.; Yang, J.; Regaieg, M.; Moncorgé, A.; Doster, F. Towards Pore Network Modelling of Spontaneous Imbibition: Contact Angle Dependent Invasion Patterns and the Occurrence of Dynamic Capillary Barriers. *Comput. Geosci.* **2020**, *24*, 951–969. [CrossRef]

56. Millington, R.J.; Quirk, J.P. Permeability of Porous Solids. *Trans. Faraday Soc.* **1961**, *57*, 1200. [CrossRef]

57. Johnson, D.B.; Hallberg, K.B. Acid Mine Drainage Remediation Options: A Review. *Sci. Total Environ.* **2005**, *338*, 3–14. [CrossRef]

58. Zvimba, J.N.; Mathye, M.; Vadapalli, V.R.K.; Swanepoel, H.; Bologo, L. Fe(II) Oxidation during Acid Mine Drainage Neutralization in a Pilot-Scale Sequencing Batch Reactor. *Water Sci. Technol.* **2013**, *68*, 1406–1411. [CrossRef]

59. Cudennec, Y.; Lecerf, A. The Transformation of Ferrihydrite into Goethite or Hematite, Revisited. *J. Solid State Chem.* **2006**, *179*, 716–722. [CrossRef]

60. Hiemstra, T.; Mendez, J.C.; Li, J. Evolution of the Reactive Surface Area of Ferrihydrite: Time, pH, and Temperature Dependency of Growth by Ostwald Ripening. *Environ. Sci. Nano* **2019**, *6*, 820–833. [CrossRef]

61. Xu, T.; Sonnenthal, E.; Spycher, N.; Pruess, K. TOUGHREACT—A Simulation Program for Non-Isothermal Multiphase Reactive Geochemical Transport in Variably Saturated Geologic Media: Applications to Geothermal Injectivity and CO_2 Geological Sequestration. *Comput. Geosci.* **2006**, *32*, 145–165. [CrossRef]

62. Kügler, S.; Cooper, R.E.; Wegner, C.-E.; Mohr, J.F.; Wichard, T.; Küsel, K. Iron-Organic Matter Complexes Accelerate Microbial Iron Cycling in an Iron-Rich Fen. *Sci. Total Environ.* **2019**, *646*, 972–988. [CrossRef]

63. Zhou, S.; Chen, S.; Yuan, Y.; Lu, Q. Influence of Humic Acid Complexation with Metal Ions on Extracellular Electron Transfer Activity. *Sci. Rep.* **2015**, *5*, 17067. [CrossRef] [PubMed]

64. Sukekava, C.F.; Downes, J.; Filella, M.; Vilanova, B.; Laglera, L.M. Ligand Exchange Provides New Insight into the Role of Humic Substances in the Marine Iron Cycle. *Geochim. Cosmochim. Acta* **2024**, *366*, 17–30. [CrossRef]

65. Costa, O.Y.A.; Raaijmakers, J.M.; Kuramae, E.E. Microbial Extracellular Polymeric Substances: Ecological Function and Impact on Soil Aggregation. *Front. Microbiol.* **2018**, *9*, 1636. [CrossRef] [PubMed]

66. Harrison, A.L.; Dipple, G.M.; Power, I.M.; Mayer, K.U. The Impact of Evolving Mineral–Water–Gas Interfacial Areas on Mineral–Fluid Reaction Rates in Unsaturated Porous Media. *Chem. Geol.* **2016**, *421*, 65–80. [CrossRef]

67. Jeen, S.-W.; Mayer, K.U.; Gillham, R.W.; Blowes, D.W. Reactive Transport Modeling of Trichloroethene Treatment with Declining Reactivity of Iron. *Environ. Sci. Technol.* **2007**, *41*, 1432–1438. [CrossRef] [PubMed]

68. Ladd, A.J.C.; Szymczak, P. Reactive Flows in Porous Media: Challenges in Theoretical and Numerical Methods. *Annu. Rev. Chem. Biomol. Eng.* **2021**, *12*, 543–571. [CrossRef] [PubMed]